

## PROBING THE PRE-REIONIZATION EPOCH WITH MOLECULAR HYDROGEN INTENSITY MAPPING

YAN GONG<sup>1</sup>, ASANTHA COORAY<sup>1</sup>, MARIO G. SANTOS<sup>2</sup>

<sup>1</sup>Department of Physics & Astronomy, University of California, Irvine, CA 92697 and

<sup>2</sup>CENTRA, Instituto Superior Técnico, Technical University of Lisbon, Lisboa 1049-001, Portugal

*Draft version June 25, 2018*

### ABSTRACT

Molecular hydrogen is now understood to be the main coolant of the primordial gas clouds leading to the formation of the very first stars and galaxies. The line emissions associated with molecular hydrogen should then be a good tracer of the matter distribution at the onset of reionization of the universe. Here we propose intensity mapping of H<sub>2</sub> line emission in rest-frame mid-infrared wavelengths to map out the spatial distribution of gas at redshifts  $z > 10$ . We calculate the expected mean intensity and clustering power spectrum for several H<sub>2</sub> lines. We find that the 0-0S(3) rotational line at a rest wavelength of 9.66  $\mu\text{m}$  is the brightest line over the redshift range of 10 to 30 with an intensity of about 5 to 10 Jy/sr at  $z \sim 15$ . To reduce astrophysical and instrumental systematics, we propose the cross-correlation between multiple lines of the H<sub>2</sub> rotational and vibrational line emission spectrum. Our estimates of the intensity can be used as a guidance in planning instruments for future mid-IR spectroscopy missions such as SPICA.

*Subject headings:* cosmology: theory — diffuse radiation — intergalactic medium — large scale structure of universe

### 1. INTRODUCTION

Existing cosmological observations show that the reionization history of the universe at  $z > 6$  is likely both complex and inhomogeneous (e.g. Haiman 2003; Choudhury & Ferrara 2006; Zaroubi 2012). While the polarization signal in the cosmic microwave background (CMB) anisotropy power spectrum constrains the total optical depth to electron scattering and the existing WMAP measurements suggest reionization happened around  $z_{\text{ri}} = 11$  (Komatsu et al. 2011), it is more likely that the reionization period was extended over a broad range of redshifts from 20 to 6. Moving beyond CMB, observations of the 21-cm spin-flip line of neutral hydrogen are now pursued to study the spatial distribution of the matter content during the epoch of reionization (e.g., Madau et al. 1997; Loeb & Zaldarriaga 2004; Gnedin & Shaver 2004). Unlike CMB, 21 cm data are useful as they provide a tomographic view of the reionization (Furlanetto et al. 2004; Santos et al. 2005). The anisotropy power spectrum of the 21 cm line emission is also a useful cosmological probe (Santos & Cooray 2006; McQuinn et al. 2006; Bowman et al. 2007; Mao et al. 2008).

While the 21 cm signal is primarily tracing the neutral hydrogen content in the intergalactic medium during reionization, line emission associated with atomic and molecular lines are of interest to study the physical properties within dark matter halos, such as gas cooling, star-formation, and the spatial distribution of first stars and galaxies. Motivated by various experimental possibilities we have studied the reionization signal associated with the CO (Gong et al. 2011), CII (Gong et al. 2012), and Lyman- $\alpha$  (Silva et al. 2012) lines. As the signal is sensitive to the metal abundance these atomic and molecular probes are more sensitive to the late stages of reionization, perhaps well into the epoch when the universe is close to full reionization and has a low 21 cm signal (Basu et al. 2004; Righi et al. 2008; Visbal & Loeb 2010; Carilli 2011; Lidz et al. 2011).

Although the end of reionization era can be effectively probed with HI, CO, CII, and Lyman- $\alpha$ , it would be also useful to have an additional probe of the onset of reionization at  $z > 10$ . Here we consider molecular hydrogen and study the signal associated with rotational and vibrational lines in the mid-IR wavelengths. Molecular hydrogen has been invoked as a significant coolant of primordial gas leading to the formation of first stars and galaxies (e.g. Haiman 1999; Bromm & Larson 2004; Glover 2005; Glover 2012). While molecular hydrogen is easily destroyed in later stages of reionization, its presence in the earliest epochs of the cosmological history can be probed with line emission experiments.

This paper is organized as follows: in the next section, we outline the calculation related to the cooling rate of H<sub>2</sub> rotational and vibrational lines. In Section 3 we present results on the H<sub>2</sub> luminosity as a function of the halo mass, while in Section 4, we discuss the mean H<sub>2</sub> intensity and clustering auto and cross power spectra. The cross power spectra between various lines are proposed as a way to eliminate the low-redshift contamination and increase the overall signal-to-noise ratio for detection. We discuss potential detectability in Section 5. We summarize our results and conclude in Section 6. We assume the flat  $\Lambda$ CDM with  $\Omega_{\text{M}} = 0.27$ ,  $\Omega_{\text{b}} = 0.046$ ,  $\sigma_8 = 0.81$ ,  $n_{\text{s}} = 0.96$  and  $h = 0.71$  for the calculation throughout the paper (Komatsu et al. 2011).

### 2. H<sub>2</sub> COOLING COEFFICIENTS

The radiation emitted by H<sub>2</sub> will be generated by the heating/cooling of the gas as the collapsing process evolves. Therefore, in order to calculate the H<sub>2</sub> luminosity, we first evaluate the cooling rate of the H<sub>2</sub> rotational and vibrational lines for optical thin and optical thick media, respectively. For hydrogen density  $n_{\text{H}} < 10^9 \text{cm}^{-3}$ , the optical depth is thin for H<sub>2</sub> emission lines. Following Hollenbach & McKee (1979), the cooling coefficient for the rotational and vibrational lines can

then be expressed as

$$\Lambda_{\text{H}_2}^{\text{r,v}}(\text{H}, \text{H}_2) = \frac{\Lambda_{\text{LTE}}^{\text{r,v}}(\text{H}, \text{H}_2)}{1 + n_{\text{cr}}^{\text{r,v}}(\text{H}, \text{H}_2)/n_{\text{H}, \text{H}_2}}, \quad (1)$$

where  $\Lambda_{\text{LTE}}^{\text{r,v}}(\text{H}, \text{H}_2)$  is the cooling coefficients of rotation or vibration at the local thermodynamic equilibrium (LTE) for the collisions with hydrogen atoms H or H<sub>2</sub>. Here  $n_{\text{cr}}^{\text{r,v}}$  is the critical density of H or H<sub>2</sub> to reach the LTE, and  $n_{\text{H}, \text{H}_2}$  is the local number density of H or H<sub>2</sub>.

In the LTE we have  $A_{\text{ul}} = C_{\text{ul}}n$  where  $A_{\text{ul}}$  is the Einstein coefficient,  $C_{\text{ul}}$  is the collisional de-excitation rate from upper to lower level, and  $n$  is the particle number density (Hollenbach & McKee 1979). Then the rotational and vibrational LTE cooling coefficient can be written as

$$\Lambda_{\text{LTE}}^{\text{r,v}}(\text{H}, \text{H}_2) = \frac{1}{n_{\text{H}, \text{H}_2}} A_J \frac{g_J}{g_{J'}} e^{-\frac{\Delta E}{kT}} \Delta E, \quad (2)$$

where  $g_J = 2J + 1$  is the statistical weight,  $J$  denotes the total angular momentum quantum number of the rotational energy level,  $A_J$  is the Einstein coefficient for  $J \rightarrow J'$  transition at the same vibrational energy level or between two vibrational energy levels, and  $\Delta E$  is the energy difference between  $E_J$  and  $E_{J'}$ . The wavenumber for each energy level and the calculation for  $E_J$  and wavelength are given in the Appendix. The values of  $A_J$  are taken from Turner et al. (1977). Note that we just consider two vibrational level transition  $v=0$  and 1 in the following calculation. The number of H<sub>2</sub> at the higher vibrational levels are much smaller than that at  $v=0$  and 1 in our case, so the strength of these lines is much weaker than those from  $v=0$  and 1. The  $n_{\text{cr}}/n$  term in Eq.(1) can be approximated by (Hollenbach & McKee 1979)

$$\frac{n_{\text{cr}}^{\text{r,v}}(\text{H}, \text{H}_2)}{n_{\text{H}, \text{H}_2}} = \frac{\Lambda_{\text{LTE}}^{\text{r,v}}(\text{H}, \text{H}_2)}{\Lambda_{n \rightarrow 0}^{\text{r,v}}(\text{H}, \text{H}_2)}, \quad (3)$$

where  $\Lambda_{n \rightarrow 0}^{\text{r,v}}$  is the low-density limit of the cooling coefficient, which can be obtained by replacing the Einstein coefficient in Eq.(2) by  $C_J^{\text{H}, \text{H}_2} n_{\text{H}, \text{H}_2}$ , i.e.

$$\Lambda_{n \rightarrow 0}^{\text{r,v}}(\text{H}, \text{H}_2) = C_J^{\text{H}, \text{H}_2} \frac{g_J}{g_{J'}} e^{-\frac{\Delta E}{kT}} \Delta E. \quad (4)$$

Here  $C_J^{\text{H}, \text{H}_2}$  is the collisional de-excitation coefficients with H or H<sub>2</sub> for  $J \rightarrow J'$  transition in the same vibrational level or between  $v=i$  and  $v=j$ , which are estimated by the fitting formula given in Hollenbach & McKee (1979) and Hollenbach & McKee (1989) (see Appendix). Using Eq.(1)-(4) we can estimate the cooling coefficient for a given H<sub>2</sub> line. Note that in Hollenbach & McKee (1979) the fitting formulae of *total* cooling coefficients for  $v=0$  rotational and  $v=0, 1$  and 2 vibrational lines are given. We denote those by  $\Lambda_{\text{H}_2}^{\text{tot,rv}}$ ,  $\Lambda_{\text{LTE}}^{\text{tot,rv}}$  and  $\Lambda_{n \rightarrow 0}^{\text{tot,rv}}$  in the cases of the total local, LTE and low-density limit cooling coefficients, respectively. Then  $n_{\text{cr}}/n$  can be expressed by  $\Lambda_{\text{LTE}}^{\text{tot,rv}}/\Lambda_{n \rightarrow 0}^{\text{tot,rv}}$ , where  $n_{\text{cr}}$  denotes the critical density when all energy level transitions are in the LTE.

For the hydrogen density  $n_{\text{H}} > 10^9 \text{cm}^{-3}$ , the optical depth is thick for the H<sub>2</sub> emission, and we have to consider the absorption effect for the H<sub>2</sub> cooling. Following Yoshida et al. (2006), we make use of the cooling efficiency, which is defined by  $f_{\text{ce}} = \Lambda_{\text{thick}}/\Lambda_{\text{thin}}$ , to evaluate

the cooling coefficient  $\Lambda_{\text{thick}}$  for the optical thick case. This reduction factor is derived from their simulations, and available for  $n_{\text{H}} \lesssim 10^{14} \text{cm}^{-3}$ , which is well within the density ranges of our calculation. The  $f_{\text{ce}}$  is about 0.02 when  $n_{\text{H}} \sim 10^{14} \text{cm}^{-3}$  and increases to about 0.1 when  $n_{\text{H}} \sim 10^{12} \text{cm}^{-3}$ . At densities below  $10^{10} \text{cm}^{-3}$  we have  $f_{\text{ce}} = 1$  (Yoshida et al. 2006).

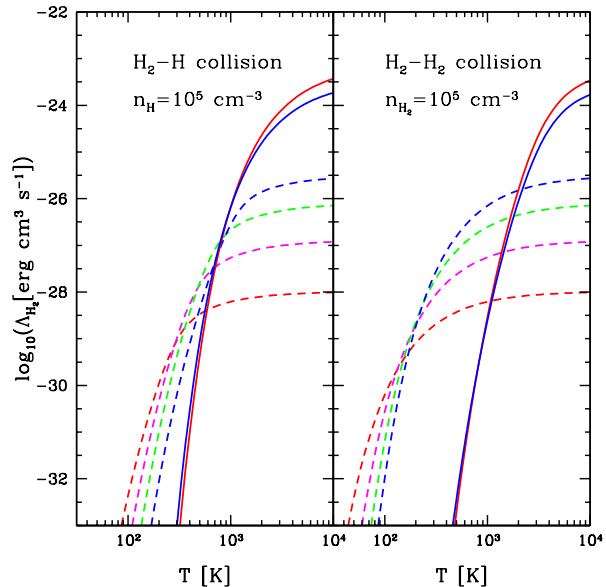


FIG. 1.— The optical-thin H<sub>2</sub> cooling coefficient vs. temperature for H<sub>2</sub>-H and H<sub>2</sub>-H<sub>2</sub> collisions at  $z = 15$ . The cooling coefficients of the rotational lines, 0-OS(0) (red), 0-OS(1) (magenta), 0-OS(2) (green) and 0-OS(3) (blue), are shown in dashed curves, and the vibrational lines, 1-OS(1) (red) and 1-0Q(1) (blue), are in solid curves.

In Fig. 1, as an example, we show the cooling coefficients for H<sub>2</sub>-H and H<sub>2</sub>-H<sub>2</sub> collisions as a function of temperature  $T$ . We assume the number density of hydrogen atom H and molecular hydrogen H<sub>2</sub> to be  $10^5 \text{cm}^{-3}$  here. The dashed curves show the cooling coefficients of the rotational lines, which are in red (0-OS(0)), magenta (0-OS(1)), green (0-OS(2)) and blue (0-OS(3)). The solid curves are for two vibrational lines 1-OS(1) in red and 1-0Q(1) in blue, respectively. As can be seen, the rotational cooling dominates at the low temperature ( $T \lesssim 10^3$  K) and the vibrational cooling dominates at high temperature ( $T \gtrsim 10^3$  K). Also, we find the  $\Lambda_{\text{H}_2}^{\text{r}}$  for H<sub>2</sub>-H<sub>2</sub> collision is generally greater than that for H<sub>2</sub>-H collision at  $T \lesssim 10^3$  K, while the  $\Lambda_{\text{H}_2}^{\text{v}}$  for H<sub>2</sub>-H<sub>2</sub> collision is less than that for H<sub>2</sub>-H collision in this temperature range. This indicates that, at low temperature, the total  $\Lambda_{\text{H}_2}^{\text{r}}$  is mainly from H<sub>2</sub>-H<sub>2</sub> collisions, and the total  $\Lambda_{\text{H}_2}^{\text{v}}$  is from H<sub>2</sub>-H collisions. At higher temperature with  $T \gtrsim 10^3$  K, the cooling rates  $\Lambda_{\text{H}_2}^{\text{r}}$  and  $\Lambda_{\text{H}_2}^{\text{v}}$  for both H<sub>2</sub>-H<sub>2</sub> and H<sub>2</sub>-H collisions are similar.

### 3. H<sub>2</sub> LUMINOSITY

We now explore the H<sub>2</sub> luminosity as a function of halo mass for rotational and vibrational lines. As discussed in the last section, the H<sub>2</sub> cooling coefficient  $\Lambda_{\text{H}_2}$  is dependent on the local gas temperature and density of hydrogen and molecular hydrogen. To evaluate H<sub>2</sub>

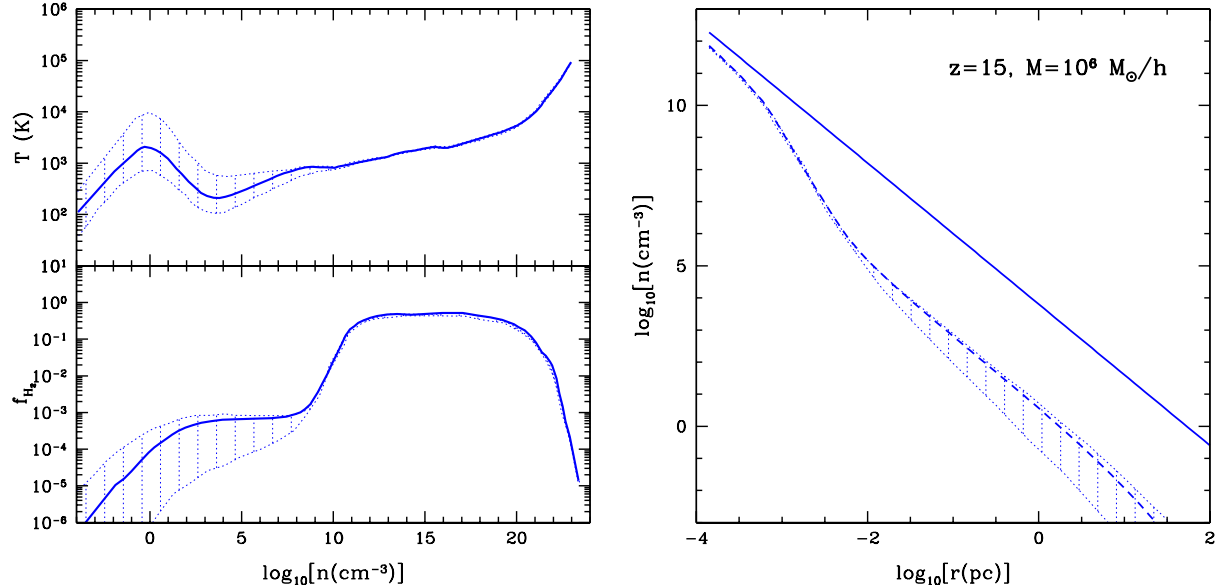


FIG. 2.— *Left*: The gas temperature  $T$  and H<sub>2</sub> fraction  $f_{\text{H}_2}$  as functions of the gas density  $n$ , which are derived from the simulation results in Omukai (2001) and Yoshida et al. (2006). The uncertainties of the gas temperature and H<sub>2</sub> fraction are shown in blue regions. *Right*: The density profile of the gas (blue solid line) and molecular hydrogen (blue dashed line) for the halo with  $M = 10^6 M_{\odot}/h$  at  $z = 15$ . The blue region shows the uncertainty of the H<sub>2</sub> density profile estimated by the uncertainty of  $f_{\text{H}_2}$  in the left panel.

luminosity vs. halo mass relation for molecular hydrogen cooling within primordial dark matter halos, we first need to know the radial profile of the gas temperature and density within dark matter halos.

Following the results from numerical simulations involving the formation of primordial molecular clouds (e.g. Omukai & Nishi 1998; Abel et al. 2000; Omukai 2001; Yoshida et al. 2006; McGreer & Bryan 2008), we assume the gas density profile as

$$\rho(r) = \rho_0 \left( \frac{r}{r_0} \right)^{-2.2}, \quad (5)$$

where we set  $r_0 = 1$  pc and  $\rho_0$  is the normalization factor which is obtained by

$$M_{\text{gas}} = 4\pi \int_0^{r_{\text{vir}}} r^2 \rho(r) dr. \quad (6)$$

Here  $M_{\text{gas}} = (\Omega_b/\Omega_M)M$  is the gas mass in the virial radius of the halo with dark matter mass  $M$ , and the  $r_{\text{vir}}$  is the virial radius which is given by

$$r_{\text{vir}} = \left[ \frac{M}{(4/3)\pi\rho_{\text{vir}}} \right]^{1/3}. \quad (7)$$

Here  $\rho_{\text{vir}}(z) = \Delta_c(z)\rho_{\text{cr}}(z)$  is the virial density,  $\rho_{\text{cr}}(z) = 3H^2(z)/(8\pi G)$  is the critical density at  $z$ ,  $H(z)$  is the Hubble parameter, and  $\Delta_c(z) = 18\pi^2 + 82z - 39z^2$  where  $x = \Omega_M(z) - 1$ .

We then derive the number density of gas by  $n(r) = n_{\text{H}}(r) + n_{\text{He}}(r)$ . Here  $n_{\text{H}}(r) = f_{\text{H}}\rho(r)/m_{\text{H}}$  is the number density of hydrogen, where  $f_{\text{H}} = 0.739$  is the hydrogen mass fraction and  $m_{\text{H}}$  is the mass of hydrogen atom. Similarly,  $n_{\text{He}}(r) = (1 - f_{\text{H}})\rho(r)/m_{\text{He}}$  is the number density of helium, where  $m_{\text{He}}$  is the mass of helium atom. Also, the temperature-density relation  $T(n)$  and the H<sub>2</sub> fraction-density relation  $f_{\text{H}_2}(n) = n_{\text{H}_2}/n$  can be derived from existing numerical simulations. Here we use

the results on  $T(n)$  and  $f_{\text{H}_2}(n)$  from Omukai (2001) and Yoshida et al. (2006), which are available for  $n \simeq 10^{-2}$  to  $10^{23} \text{ cm}^{-3}$  as shown in the left panel of Fig. 2. The uncertainties of the gas temperature and H<sub>2</sub> fraction are shown in blue regions. These uncertainties are evaluated based on the differences in the far-ultraviolet radiation background from the first stars and quasars (Omukai 2001).

As can be seen, the gas temperature does not monotonously increase with the gas density. For instance, it drops from  $T \sim 2000$  to 200 K between  $n \simeq 1$  and  $10^4 \text{ cm}^{-3}$  where molecular hydrogen density is rising to  $f_{\text{H}_2} \sim 10^{-3}$ . This indicates that H<sub>2</sub> cooling is starting to become important in this gas density range. At  $n \simeq 10^4 \text{ cm}^{-3}$ , H<sub>2</sub> cooling saturates and turns into the cooling at the LTE. For  $n = 10^{10} \sim 10^{11} \text{ cm}^{-3}$ , almost all of gas particles become molecular hydrogen due to the efficient H<sub>2</sub> three-body reaction (Yoshida et al. 2006), and we find  $f_{\text{H}_2} \simeq 0.5$  by definition. At  $n \simeq 10^{20} \text{ cm}^{-3}$  with  $T \simeq 10^4$  K, H<sub>2</sub> begins to dissociate and the fraction drops quickly to  $f_{\text{H}_2} < 10^{-5}$  when  $n \simeq 10^{23} \text{ cm}^{-3}$  and  $T \simeq 10^5$  K.

Next, with the help of Eq. (5), we can evaluate the gas temperature and H<sub>2</sub> fraction as a function of the halo radius, i.e.  $T(r)$  and  $f_{\text{H}_2}(r)$ . Once these are established, we can derive  $n_{\text{H}_2}(r)$ ,  $n_{\text{H}}(r)$  and  $\Lambda_{\text{H}_2}^{\text{r,v}}(r)$  which are needed for the H<sub>2</sub> luminosity calculation. In the right panel of Fig. 2, we show the density profile of the gas and molecular hydrogen in blue solid and dashed lines for a dark matter halo with  $M = 10^6 M_{\odot}/h$  at  $z = 15$ . The blue region shows the uncertainty of the H<sub>2</sub> density profile which is derived by the uncertainty of  $f_{\text{H}_2}$  in the left panel of Fig. 2. The gas density profile is a straight line with a slope of -2.2 as indicated by Eq. (5). On the other hand, the density profile of molecular hydrogen has a more complex shape which is dependent on the relation between  $f_{\text{H}_2}$  and gas density  $n$ . For the outer layer of the gas cloud ( $r > 10^{-2}$  pc), gas density is less than

$10^5 \text{ cm}^{-3}$  and  $f_{\text{H}_2} \lesssim 4 \times 10^{-4}$ . Here  $\text{H}_2$  density is much smaller than the gas density. For the inner region with  $10^{-3.5} < r < 10^{-2}$  pc, we find  $10^5 < n < 10^{11} \text{ cm}^{-3}$  and  $f_{\text{H}_2}$  begins to rise up quickly with  $n_{\text{H}_2}$  becoming close to the gas density. For the inner-most region at  $r < 10^{-3.5}$  pc, the gas density is greater than  $10^{11} \text{ cm}^{-3}$ , and  $f_{\text{H}_2} \simeq 0.5$  so that almost all of hydrogen end up forming molecular hydrogen.

The luminosity of the  $\text{H}_2$  rotational or vibrational lines can then be estimated by

$$L_{\text{H}_2}^{\text{r,v}}(M, z) = 4\pi \int_0^{r_{\text{vir}}} dr r^2 n_{\text{H}_2}^{\text{r,v}}(r) \times [n_{\text{H}}(r)\Lambda_{\text{H}_2}^{\text{r,v}}(\text{H}) + n_{\text{H}_2}(r)\Lambda_{\text{H}_2}^{\text{r,v}}(\text{H}_2)], \quad (8)$$

where  $n_{\text{H}_2}^{\text{r,v}}(r)$  is the number density of the molecular hydrogen that can emit at a given rotational or vibrational line at  $r$ . We first evaluate the total  $n_{\text{H}_2}$  at  $v=0$  and 1 states by condensing all the rotational levels at a given vibrational state to be a single vibrational level,  $n_i = n_{i-1} \exp[-\Delta E_{i,i-1}/(kT)]$  where  $i = 1$ . Here  $g_0 = g_1 = 1$  for  $v=0$  and 1, respectively, and  $\Delta E_{10}/k \simeq 5860 \text{ K}$  (Hollenbach & McKee 1979). Then we estimate  $n_{\text{H}_2}$  for a given rotational energy level  $J$  in a vibrational level  $i$  by  $n_J = n_{J'} (g_J/g_{J'}) \exp[-\Delta E_{J,J'}/(kT)]$ . The fractions of the ortho and para states of total  $n_{\text{H}_2}$  are assumed to be 0.75 and 0.25, respectively, in our calculation.

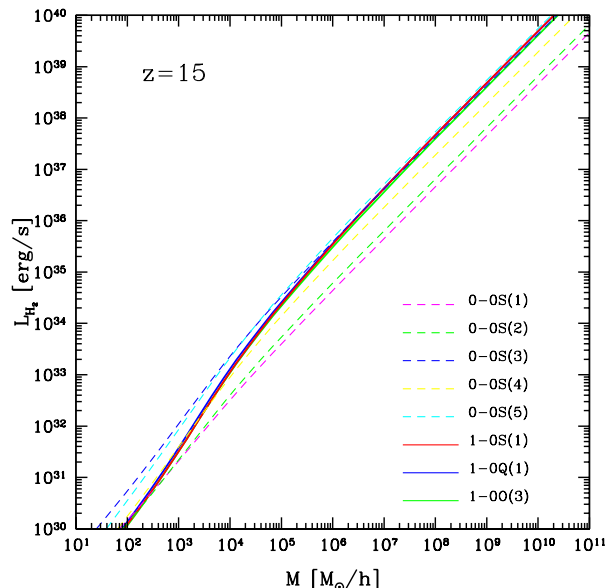


FIG. 3.—  $\text{H}_2$  line luminosity vs. dark matter halo mass  $M$  at  $z = 15$ . To avoid crowding we select the first eight strongest lines to show here. In our calculations we find that the 0-0S(3) is the most luminous line, while lines such as 0-0S(5), 1-0S(1), 1-0Q(1) and 1-0O(3), are comparable for high halo masses.

In Fig. 3, we show  $\text{H}_2$  luminosity of several lines as a function of the halo mass at  $z = 15$ . In these lines, we find that the rotational line 0-0S(3) at a rest-frame wavelength of  $9.66 \mu\text{m}$  is the most luminous one. Other lines, such as 0-0S(5), 1-0S(1), 1-0Q(1) and 1-0O(3), are also strong for halos with high mass (see also Table 1). As can be seen, for low halo masses with  $M \lesssim 10^5 M_{\odot}/h$ , the rotational lines are stronger than the vibrational lines.

This is caused by the fact that the halos with low masses have lower mean gas temperature than the massive halos, and the rotational cooling is stronger than the vibrational cooling in such halos, as indicated by Fig. 1.

#### 4. $\text{H}_2$ INTENSITY AND POWER SPECTRUM

Given the relation between  $\text{H}_2$  luminosity and the dark matter halo mass, the mean intensity of the  $\text{H}_2$  lines can be expressed as (Visbal & Loeb 2010; Gong et al. 2011)

$$\bar{I}_{\text{H}_2}(z) = \int_{M_{\text{min}}}^{\infty} dM \frac{dn}{dM}(M, z) \frac{L_{\text{H}_2}(M, z)}{4\pi D_L^2} y(z) D_A^2, \quad (9)$$

where we choose  $M_{\text{min}} = 10 M_{\odot}/h$ ,  $dn/dM$  is the halo mass function (Sheth & Tormen 1999),  $y(z) = d\chi/d\nu = \lambda_{\text{H}_2}(1+z)^2/H(z)$  when  $\chi$  is the comoving distance and  $\lambda_{\text{H}_2}$  is the wavelength of  $\text{H}_2$  lines in the rest frame. Our results are not strongly sensitive to the exact value of minimum halo mass. If we increase the minimum halo mass to the level of  $10^6 M_{\odot}/h$ , the mean intensity we present here decrease by a factor of  $\sim 2$  for all  $\text{H}_2$  lines.

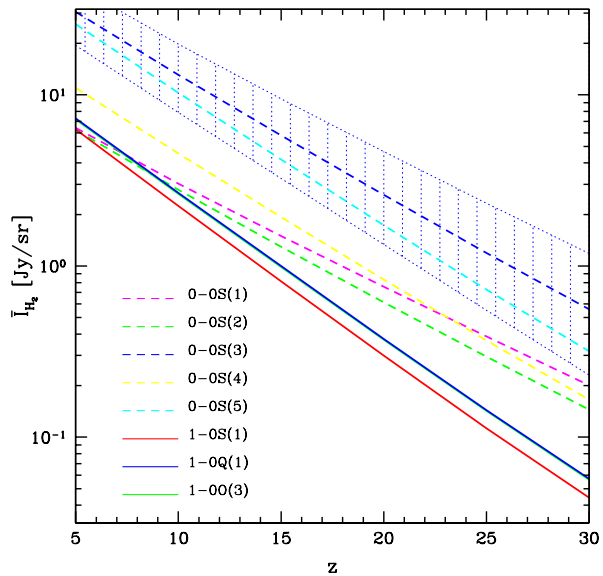


FIG. 4.— The mean intensity of  $\text{H}_2$  lines as a function of redshift  $z$ . The blue region is the uncertainty of the intensity of 0-0S(3) line which is estimated from uncertainties in the gas temperature and  $f_{\text{H}_2}$  shown on the left panel of Fig. 2. We find the 0-0S(3) line is the most luminous line for  $10 \leq z \leq 30$ , and the slopes of the relations for the vibrational lines are generally steeper than the rotational lines. Note that for  $5 \leq z \leq 10$  we do not consider the dissociation effect of the molecular hydrogen by Pop II and Pop III stars.

In Fig. 4, we show the mean intensity of the eight strongest  $\text{H}_2$  lines as a function of redshift  $z$ . The uncertainty in the intensity of the 0-0S(3) line is shown with the shaded blue region, which is derived from uncertainties in the gas temperature and  $f_{\text{H}_2}$  in the left panel of Fig. 2. We find that the mean intensity of the 0-0S(3) rotational line is the strongest for  $10 \leq z \leq 30$ . This is because the 0-0S(3) line is the most luminous line for low-mass halos, which have a higher number density and dominate the halo distribution at  $z = 15$ . Also, the slopes of the intensity-redshift relation for the vibrational lines are steeper than that of the rotational lines,

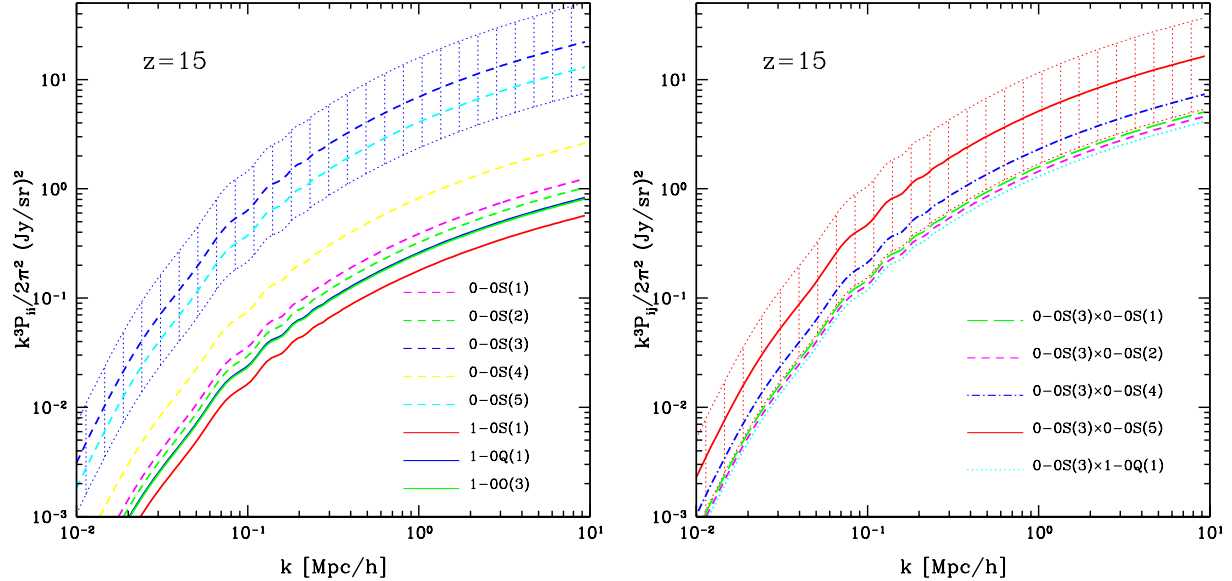


FIG. 5.— *Left*: The  $\text{H}_2$  clustering auto power spectrum at  $z = 15$ . Eight brightest lines are selected to show here. The blue region is the uncertainty on the clustering power spectrum for the 0-OS(3) line and is derived from the uncertainties in the gas temperature and  $f_{\text{H}_2}$ . *Right*: The  $\text{H}_2$  clustering cross power spectrum at  $z = 15$ . Here we choose the strongest 0-OS(3) line to cross correlate with next five strong lines. The propose cross-correlation effectively eliminates the astrophysical line confusion from low-redshift sources and other mid-IR lines. The red region shows the uncertainty for 0-OS(3) $\times$ 0-OS(5), which is also estimated from the uncertainties in the gas temperature and  $f_{\text{H}_2}$ .

since they have steeper slopes for cooling coefficients with temperature as shown in Fig. 1. However, we find the difference in slopes to become smaller for the rotational lines as  $J$  is increased, indicating that the high- $J$  rotational lines have similar slopes with cooling coefficient when compared to that of the vibrational lines.

We note here that we do not consider the dissociation effect of the molecular hydrogen by Pop II and Pop III stars in our calculation. We expect the formation of these stars to be important at  $z < 10$  and that there would be significant amount of  $\text{H}_2$  that should be dissociated by the UV photons emitting from the first stars. Thus  $\text{H}_2$  emission could be suppressed significantly at  $z \leq 10$ . At  $z \sim 15$ , there should still be some dissociation but we ignore it to obtain a safe upper limit estimate on the expected  $\text{H}_2$  intensity for experimental planning purposes.

Next we can derive the clustering power spectrum of the  $\text{H}_2$  lines, writing the intensity as  $I_{\text{H}_2}(z) = \bar{I}_{\text{H}_2}[1 + b_{\text{H}_2}\delta(\mathbf{x})]$ . Here  $b_{\text{H}_2}$  is the average  $\text{H}_2$  clustering bias, which can be estimated from

$$\bar{b}_{\text{H}_2}(z) = \frac{\int_{M_{\min}}^{\infty} dM \frac{dn}{dM} L_{\text{H}_2} b(M, z)}{\int_{M_{\min}}^{\infty} dM \frac{dn}{dM} L_{\text{H}_2}}, \quad (10)$$

where  $b(M, z)$  is the bias factor for dark matter halos with mass  $M$  at  $z$  (Sheth & Tormen 1999). The  $\text{H}_2$  clustering auto power spectrum is then given by

$$P_{\text{H}_2}^{\text{clus}}(k, z) = \bar{I}_{\text{H}_2}^2 \bar{b}_{\text{H}_2}^2 P_{\delta\delta}(k, z), \quad (11)$$

where  $P_{\delta\delta}(k, z)$  is the matter power spectrum, which is obtained from a halo model (Cooray & Sheth 2002). At a high redshift as  $z = 15$ , the structure of matter distribution is extremely linear and the 2-halo term dominates the power spectrum.

We can also estimate the shot-noise power spectrum for the  $\text{H}_2$  lines, which is caused by the discretization of

TABLE 1  
THE WAVELENGTH,  $\Delta J = J - J'$ , SPONTANEOUS EMISSION COEFFICIENT  $A_J$ , MEAN BIAS AND MEAN INTENSITY FOR THE  $\text{H}_2$  ROTATIONAL AND VIBRATIONAL LINES AT  $z = 15$ .

$\text{H}_2$ line	$\lambda$ ( $\mu\text{m}$ )	$\Delta J$	$A_J$ ( $\text{s}^{-1}$ )	$b_{\text{H}_2}$	$\bar{I}_{\text{H}_2}$ (Jy/sr)
0-OS(0)	28.2	+2	$2.94 \times 10^{-11}$	$2.6^{+0.4}_{-0.1}$	$0.08^{+0.28}_{-0.06}$
0-OS(1)	17.0	+2	$4.76 \times 10^{-10}$	$2.8^{+0.3}_{-0.2}$	$1.52^{+4.87}_{-2.20}$
0-OS(2)	12.3	+2	$2.76 \times 10^{-9}$	$3.0^{+0.2}_{-0.3}$	$1.32^{+2.20}_{-0.61}$
0-OS(3)	9.66	+2	$9.84 \times 10^{-9}$	$3.1^{+0.2}_{-0.2}$	$5.90^{+3.60}_{-2.64}$
0-OS(4)	8.03	+2	$2.64 \times 10^{-8}$	$3.2^{+0.2}_{-0.1}$	$1.97^{+0.94}_{-0.92}$
0-OS(5)	6.91	+2	$5.88 \times 10^{-8}$	$3.3^{+0.2}_{-0.2}$	$4.26^{+2.15}_{-2.1}$
0-OS(6)	6.11	+2	$1.14 \times 10^{-7}$	$3.4^{+0.2}_{-0.2}$	$0.78^{+0.52}_{-0.40}$
0-OS(7)	5.51	+2	$2.00 \times 10^{-7}$	$3.5^{+0.2}_{-0.3}$	$1.05^{+1.02}_{-0.54}$
0-OS(8)	5.05	+2	$3.24 \times 10^{-7}$	$3.6^{+0.3}_{-0.6}$	$0.13^{+0.22}_{-0.07}$
0-OS(9)	4.69	+2	$4.90 \times 10^{-7}$	$3.8^{+0.2}_{-0.9}$	$0.13^{+0.44}_{-0.07}$
0-OS(10)	4.41	+2	$7.03 \times 10^{-7}$	$4.0^{+0.2}_{-1.3}$	$0.01^{+0.11}_{-0.01}$
0-OS(11)	4.18	+2	$9.64 \times 10^{-7}$	$4.2^{+0.2}_{-1.3}$	$0.01^{+0.23}_{-0.01}$
1-OS(0)	2.22	+2	$2.53 \times 10^{-7}$	$3.4^{+0.2}_{-0.7}$	$0.24^{+0.07}_{-0.12}$
1-OS(1)	2.12	+2	$3.47 \times 10^{-7}$	$3.5^{+0.2}_{-0.7}$	$0.83^{+3.06}_{-0.42}$
1-0Q(1)	2.41	0	$4.29 \times 10^{-7}$	$3.4^{+0.2}_{-0.5}$	$1.00^{+1.96}_{-0.50}$
1-0O(3)	2.80	-2	$4.23 \times 10^{-7}$	$3.4^{+0.2}_{-0.5}$	$0.99^{+1.96}_{-0.50}$

the spatial distribution of the primordial clouds,

$$P_{\text{H}_2}^{\text{shot}}(z) = \int_{M_{\min}}^{\infty} dM \frac{dn}{dM} \left[ \frac{L_{\text{H}_2}}{4\pi D_L^2} y(z) D_A^2 \right]^2. \quad (12)$$

In Table 1, we tabulate the rest-frame wavelength,  $\Delta J = J - J'$ , spontaneous emission coefficient  $A_J$ , mean bias and mean intensity for 13 rotational and 4 vibrational lines at  $z = 15$ . The uncertainties of the mean bias and intensity are evaluated by the uncertainty of the gas temperature and  $f_{\text{H}_2}$  from the simulations. We find that the mean intensity of the 0-OS(3) rotational line at a rest wavelength of 9.66  $\mu\text{m}$  is the strongest among these lines, with a value of around 6 Jy/sr and a range from 3 to 10 Jy/sr. The other rotational lines such as 0-

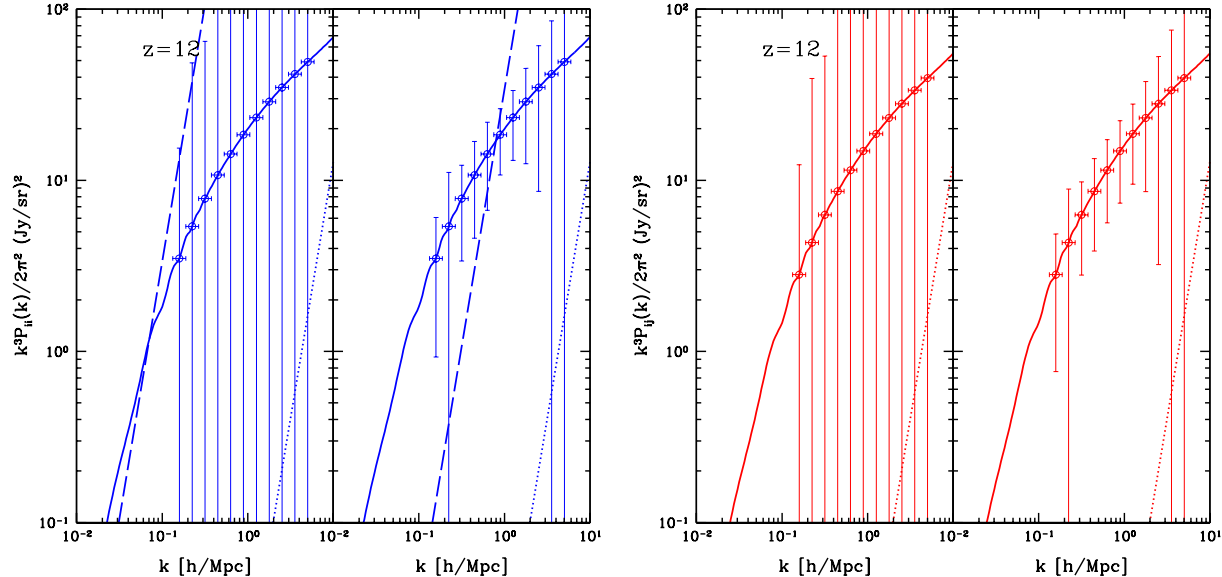


FIG. 6.— The auto power spectrum of the 0-0S(3) line (left panel) and the cross power spectrum of the 0-0S(3)×0-0S(5) (right panel) at  $z = 12$  with the errors estimated for a SPICA/BLISS-like and  $10\times$  better SPICA/BLISS-like surveys in each plot. The noise power spectrum and shot-noise power spectrum are shown in long-dashed and dotted lines, respectively.

0S(5), 0-0S(4), 0-0S(1) and 0-0S(2) are also bright with total intensities of  $\sim 4.3, 2.0, 1.5$  and  $1.3$  Jy/sr, respectively, at  $z = 15$ . The vibrational lines 1-0S(1), 1-0Q(1) and 1-0O(3) have low mean intensities at the level of 0.83, 1.0 and 0.99 Jy/sr, respectively. The mean bias factor of these lines lies between 2.6 (for 0-0S(0)) and 4.2 (for 0-0S(11)), and the bias factors of the rotational lines at higher rotational energy level are higher than that at lower level. This is because the lines with high  $J$  are stronger at higher mass halos where the temperature is larger.

In the left panel of Fig. 5, the clustering auto power spectrum of eight  $H_2$  lines at  $z = 15$  are shown. We find that the shot noise power spectrum  $P_{\text{shot}}$  is relatively small compared to the clustering power spectrum  $P_{\text{clus}}$ , and would not affect the  $P_{\text{clus}}$  at the scales of interest. This is easy to understand if we notice that the halo mass function is dominated by halos with low masses which are more abundant.

We also calculate the cross correlation between two different  $H_2$  lines. Such a cross-correlation will reduce the astrophysical contamination from the other sources, such as low-redshift emission lines from star-forming galaxies, including  $63 \mu\text{m}$  [OI] and  $122 \mu\text{m}$  [NII], among others. At  $z \sim 15$ , the dominant rotational line 0-0S(3) would be observed at a wavelength of  $155 \mu\text{m}$ . Such a line would be contaminated by, for example,  $z \sim 0.3$  galaxies emitting [NII]. Thus the auto power spectrum would be higher than what we have predicted given that the line intensities of [NII] are higher than  $H_2$  lines. To avoid this astrophysical line confusion we propose a cross-correlation between two rotational or rotational and vibrational lines of the  $H_2$  line emission spectrum.

The cross clustering and shot-noise power spectrum for such two  $H_2$  lines  $i$  and  $j$  can be evaluated as

$$P_{\text{clus}}^{ij} = \bar{I}_{H_2}^i \bar{I}_{H_2}^j \bar{b}_{H_2}^i \bar{b}_{H_2}^j P_{\delta\delta} \quad (13)$$

and

$$P_{\text{shot}}^{ij} = \int_{M_{\text{min}}}^{\infty} dM \frac{dn}{dM} \frac{L_{H_2}^i}{4\pi D_L^2} \frac{L_{H_2}^j}{4\pi D_L^2} y^i(z) D_A^2 y^j(z) D_A^2, \quad (14)$$

respectively. From these equations, we find that the cross power spectrum should have a similar magnitude to the auto power spectrum. The clustering cross power spectra  $P_{ij}^{\text{clus}}$  for several  $H_2$  lines at  $z = 15$  are shown in the right panel of Fig. 5. We choose the strongest 0-0S(3) line to cross correlate with the other 5 bright lines, i.e. 0-0S(1), 0-0S(2), 0-0S(4), 0-0S(5) and 1-0Q(1). We find that the 0-0S(3)×0-0S(5) is the largest cross power spectrum since they are brightest two lines. At  $z \sim 15$ , then we would be cross-correlating the wavelength regimes around 110 and  $155 \mu\text{m}$ . A search for mid-IR lines revealed no astrophysical confusions from low redshifts that overlap in these two wavelengths at the same redshift. Thus, while low redshift lines will easily dominate the auto power spectra of  $H_2$  lines, the cross power spectrum will be independent of the low-redshift confusions. In addition to reducing the astrophysical confusions, the cross power spectra also have the advantage that it can minimize instrumental systematics and noise, depending on the exact design of an experiment.

## 5. DETECTABILITY

In this section we investigate the possibility to detect these lines based on current or future instruments. We assume a SPICA-like<sup>1</sup> survey with 3.5 m aperture diameter,  $0.1 \text{ deg}^2$  survey area, 10 GHz band width,  $R=700$  frequency resolution, 100 spectrometers, and 250 hours total integration time and noise per detector  $\sigma_{\text{pix}} = 10^6 \text{ Jy}\sqrt{\text{s}}/\text{sr}$  at  $100 \mu\text{m}$ . Such an instrument corresponds to the latest design of the mid-IR spectrometer, BLISS, from SPICA (Bradford et al. 2010).

<sup>1</sup> <http://sci.esa.int/science-e/www/area/index.cfm?fareaid=105>

In Fig. 6, we show the errors of the auto power spectrum of 0-OS(3) line and cross power spectrum of 0-OS(3) $\times$ 0-OS(5) at  $z=12$  for two cases, a SPICA/BLISS-like and an experiment with  $10\times$  better sensitivity than with the current design of SPICA/BLISS with  $\sigma_{\text{pix}} = 10^5 \text{ Jy}\sqrt{\text{s}}/\text{sr}$ . The noise power spectrum from the instrument and shot-noise power spectrum caused by the discrete distribution of the gas clouds are also shown in long-dashed and dotted lines, respectively. We estimate the noise power spectrum and the errors by the same method described in Gong et al. (2012). We find the signal to noise ratio S/N is 0.2 and 5.2 for the auto power spectrum of 0-OS(3) line in the two cases, and S/N = 0.1 and 4.5 for the cross power spectrum of 0-OS(3) $\times$ 0-OS(5). This indicates that the current version of SPICA/BLISS does not have the sensitivity to measure the intensity fluctuation of the  $\text{H}_2$  lines at a redshift around  $z = 12$ . We find that the noise requirements suggest an instrument that is roughly 10 times better in detector noise than current SPICA/BLISS for a reliable detection.

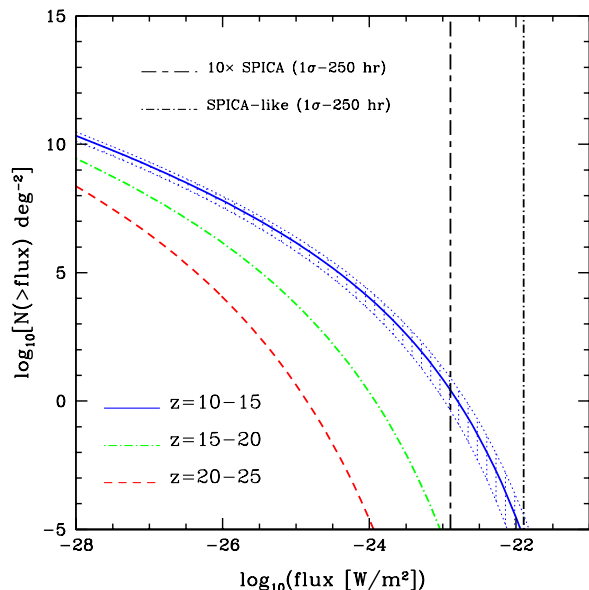


FIG. 7.— The number counts of  $\text{H}_2$  sources for 0-OS(3) line, per  $\text{deg}^2$  with flux greater than a given value for different redshift ranges. The uncertainty for  $z = 10$  to 15 is shown in blue region, which is estimated by the uncertainties of the gas density and  $f_{\text{H}_2}$ . We also show the flux limit of a SPICA/BLISS pencil-beam survey and another with  $10\times$  better instrumental sensitivity, for a  $1\sigma$  detection with 250 hours of integration time.

In addition to measuring the intensity fluctuations we also explore the detection of the  $\text{H}_2$  point sources at high redshifts. In Fig. 7, we estimate the number of the  $\text{H}_2$  sources, for 0-OS(3) line per  $\text{deg}^2$  with flux greater than a given value for three redshift ranges  $10 \leq z \leq 15$ ,  $15 \leq z \leq 20$  and  $20 \leq z \leq 25$ . The uncertainty for  $10 \leq z \leq 15$  is shown as an example which is derived from the uncertainties of the simulations. The flux limits of a pencil-beam survey with a SPICA/BLISS-like instrument and a  $10\times$  better SPICA/BLISS surveys for  $1\sigma$  detection with 250 hours of total integration time are also shown in vertical dash-dotted lines. We find it is hard to detect the  $\text{H}_2$  sources even for the redshift range

$10 \leq z \leq 15$  using the SPICA/BLISS-like experiment. The number counts of the  $\text{H}_2$  sources at  $10 \leq z \leq 15$  is around  $10^{-5}$  per  $\text{deg}^2$  for the SPICA/BLISS-like survey. For the instrument that is 10 times better in sensitivity than SPICA, we find that, in this first estimate of  $\text{H}_2$  counts, that we can aim to get about 10 sources per  $\text{deg}^2$  at  $10 \leq z \leq 15$ .

## 6. DISCUSSION AND CONCLUSION

In this paper, we propose intensity mapping of  $\text{H}_2$  rotational and vibrational lines to detect the primordial gas distribution at large scales during the pre-reionization epochs at  $z > 10$ . At such high redshifts the molecular hydrogen takes the role of main coolant that leads to the formation of first stars and galaxies and the detection of  $\text{H}_2$  power spectrum can reveal details about the halo mass scales which first form stars and galaxies in the universe.

We first estimate the cooling rates for both  $\text{H}_2$  rotational and vibrational lines with the help of fitting results from Hollenbach & McKee (1979) and Hollenbach & McKee (1989). We find the rotational lines are dominant at low gas temperature, while the vibrational lines are stronger at high gas temperature. Also, the slope of the cooling coefficient-temperature relation for the vibrational lines is steeper than that for the rotational lines. We then derive the gas number density, temperature and  $\text{H}_2$  fraction as functions of the halo radius and estimate the relation of the  $\text{H}_2$  luminosity and halo mass.

Next we calculate the mean intensity for several  $\text{H}_2$  lines at different redshifts and find the 0-OS(3) is the brightest line for  $5 \leq z \leq 30$  ( $\simeq 5.9 \text{ Jy}/\text{sr}$  at  $z=15$ ). Note that we do not consider the dissociation effects of the  $\text{H}_2$  by the Pop III and Pop II stars at  $5 \leq z \leq 10$  that could suppress the  $\text{H}_2$  emission significantly in this redshift range. Finally, we evaluate the clustering and shot-noise of auto and cross power spectrum for the  $\text{H}_2$  lines at  $z=15$ . We find the 0-OS(3) $\times$ 0-OS(5) is the strongest cross power spectrum at  $z = 15$ . We propose such a cross-power spectrum for an experimental measurement as it has the advantage that it can minimize astrophysical line confusion from low-redshift galaxies.

In order to consider potential detection of these mid-IR molecular lines we evaluate the errors of the  $\text{H}_2$  auto and cross power spectrum at  $z = 12$  for a SPICA/BLISS-like and a design that is  $10\times$  better than the current instrumental parameters. We find the S/N for the  $z = 12$  cross power spectrum detection is around 0.1 and 5 for these two experiments. We also estimate the detectability of  $\text{H}_2$  point sources over different redshift ranges. We find a SPICA/BLISS-like instrument is not able to detect  $\text{H}_2$  sources for  $z > 10$ , but an instrument with  $10\times$  better sensitivity than SPICA/BLISS should be able to detect about 10 sources per  $\text{deg}^2$  for  $10 < z < 15$ . We encourage further work on this topic to fully account for dissociation as stars and galaxies form and additional formation mechanisms, such as shock heating, that results in  $\text{H}_2$  line emission from low-redshift galaxies.

This work was supported by NSF CAREER AST-0645427. MGS acknowledges support from FCT-Portugal under grant PTDC/FIS/100170/2008. We thank Matt Bradford for helpful discussions and ques-

TABLE 2  
THE WAVENUMBERS IN  $\text{cm}^{-1}$  OF  $\text{H}_2$  ENERGY LEVELS FOR  $J=0,\dots,13$  AT  $v=0$  AND 1.

$J$	$v=0$	$v=1$
0	0.00	4161.14
1	118.50	4273.75
2	354.35	4497.82
3	705.54	4831.41
4	1168.78	5271.36
5	1740.21	5813.95
6	2414.76	6454.28
7	3187.57	7187.44
8	4051.73	8007.77
9	5001.97	8908.28
10	6030.81	9883.79
11	7132.03	10927.12
12	8298.61	12031.44
13	9523.82	13191.06

tions that motivated this paper.

#### REFERENCES

- Abel, T., Bryan, G. L., & Norman, M. L. 2000, *ApJ*, 540, 39  
 Basu, K., Hernandez-Monteagudo, C., & Sunyaev, R. A. 2004, *A&A*, 416, 447  
 Bowman, J. D., Morales, M. F., & Hewitt, J. N. 2007, *ApJ*, 661, 1  
 Bradford, M. et al. 2010, U.S. Participation in the JAXA-led SPICA Mission: The Background-Limited Infrared-Submillimeter Spectrograph (BLISS).  
 Bromm V., & Larson, R. B. 2004, *Annu. Rev. Astron. Astrophys.*, 42, 79-118  
 Carilli, C. L. 2011, *ApJ*, 730, L30  
 Choudhury, T. R., & Ferrara, A. 2006, *arXiv:astro-ph/0603149*  
 Cooray, A., & Sheth, R. 2002, *Phys.rept.*, 372, 1  
 Dabrowski, I. 1984 *Canadian J. Phys.*, 62, 1639  
 Furlanetto, S. R., Zaldarriaga, M., & Hernquist, L. 2004, *ApJ*, 613, 16  
 Glover, S. C. O. 2005, *Space Sci.Rev.*, 117, 445  
 Glover, S. C. O. 2012, *arXiv:1209.2509*  
 Gnedin, N. Y., & Shaver, P. A. 2004, *ApJ*, 608, 611  
 Gong, Y. et al. 2011, *ApJ*, 728, L46  
 Gong, Y. et al. 2012, *ApJ*, 745, 49  
 Haiman, Z. 1999, *Adv.Space Res.*, 23, 915-924  
 Haiman, Z. 2003, *Coevolution of Black Holes and Galaxies*, from the Carnegie Observatories Centennial Symposia. Published by Cambridge University Press, as part of the Carnegie Observatories Astrophysics Series. Edited by L. C. Ho, 2004, p. 67.  
 Hollenbach, D., & Mckee, C. F. 1979, *ApJS*, 41, 555  
 Hollenbach, D., & Mckee, C. F. 1989, *ApJ*, 342, 306  
 Komatsu, E., Smith, K. M., Dunkley, J., et al. 2011, *ApJS*, 192, 18  
 Loeb, A., & Zaldarriaga, M. 2004, *PRL*, 92, 211301  
 Lidz, A. et al. *arXiv.org:1104.4800*  
 Madau, P., Meiksin, A., & Rees, M. J. 1997, *ApJ*, 475, 429.  
 Mao, Y., Tegmark, M., McQuinn, M., Zaldarriaga, M., & Zahn, O. 2008, *PRD*, 78, 023529  
 McGreer, I. D., & Bryan, G. L. 2008, 685, 8  
 McQuinn, M., Zahn, O., Zaldarriaga, M., Hernquist, L., & Furlanetto, S. R. 2006, *ApJ*, 653, 815  
 Omukai, K., & Nishi, R. 1998, *ApJ*, 508, 141  
 Omukai, K. 2001, *ApJ*, 546, 635  
 Righi, M., Hernandez-Monteagudo, C., & Sunyaev, R. A. 2008, *A&A*, 2, 489  
 Santos, M. G., Cooray, A., & Knox, L. 2005, *ApJ*, 625, 575  
 Santos, M., & Cooray, A. 2006, *PRD*, 74, 083517  
 Silva, M. et al. 2012, *ApJ* in press, *arXiv.org:1205.1493*  
 Turner, J., Kirby-Docken, K., & Dalgarno, A. 1977, *ApJS*, 35, 281  
 Visbal, E., & Loeb, A. 2010, *J. Cosmol. Astropart. Phys.*, JCAP11(2010)016  
 Yoshida, N., Kazuyuki, O., Hernquist, K., & Abel, T. 2006, *ApJ*, 652, 6  
 Zaroubi, S. 2012, *arXiv:1206.0267*

#### APPENDIX

Here we list the fitting formulae of the collisional de-excitation coefficients  $C_J^{\text{H},\text{H}_2}$  for both  $\text{H}_2$ -H and  $\text{H}_2$ - $\text{H}_2$  collision from Hollenbach & McKee (1979) and Hollenbach & McKee (1989). For the rotational cooling in  $v=0$ , we have

$$C_J^{\text{H}}(T) = \left( \frac{10^{-11}T_3^{0.5}}{1 + 60T_3^{-4}} + 10^{-12}T_3 \right) \left\{ 0.33 + 0.9 \exp \left[ - \left( \frac{J - 3.5}{0.9} \right)^2 \right] \right\} \text{cm}^3\text{s}^{-1}, \quad (1)$$

$$C_J^{\text{H}_2}(T) = (3.3 \times 10^{-12} + 6.6 \times 10^{-12}T_3) \left\{ 0.276J^2 \exp \left[ - \left( \frac{J}{3.18} \right)^{1.7} \right] \right\} \text{cm}^3\text{s}^{-1}, \quad (2)$$

where  $T_3 = T/1000$  K, and  $T$  is the gas temperature. For the vibrational cooling between  $v=1$  and 0, we have

$$C_{10}^{\text{H}}(T) = 1.0 \times 10^{-12} T^{0.5} \exp[-(1000/T)] \text{cm}^3\text{s}^{-1}, \quad (3)$$

$$C_{10}^{\text{H}_2}(T) = 1.4 \times 10^{-12} T^{0.5} \exp[-18100/(T + 1200)] \text{cm}^3\text{s}^{-1}. \quad (4)$$

The wavenumbers  $k = 1/\lambda$  of  $\text{H}_2$  energy levels for  $J=0,\dots,13$  at  $v=0$  and 1 from Dabrowski (1984) are listed in Table 2. We can get the energy for each level by  $E_J = h_P c k$ , where  $h_P$  is the Planck constant and  $c$  is the speed of light. The wavelengths of the  $\text{H}_2$  line hence could be derived by  $\lambda_{\text{H}_2} = h_P c / (E_J - E_{J'})$ .